Tuning the Surface Properties of CuO Films Using the Precursor Aging Approach for Enhanced Photoelectrocatalytic Reactions

Pannan I. Kyesmen,* Nolwazi Nombona, and Mmantsae Diale*

The surface properties of semiconductors have a significant influence on their photoelectrocatalytic efficiency. This research presents a precursor aging method for tuning the surface properties of CuO films, for enhanced catalytic response. A precursor solution made using copper acetate, polyethylene glycol (PEG) 400, and diethanolamine, and aged for 1, 40, 80, 120, 150, 180, and 250 days is used in each case to fabricate CuO photocathodes via the dip-coating method. The films fabricated using the 1-day-old precursor reveal compact and homogeneous nanoparticles. The films eventually get tuned to yield highly porous and rougher surfaces after aging the precursors for 180–250 days. The film's bandgap decreases by 9% after 180–250 days of precursor aging. Photocathodes prepared using the 180-day-old precursor produce the optimum photocurrent density of 1.6 mA cm^{-2} at 0.35 V versus reversible hydrogen electrode (RHE), representing a 196% increase relative to the films fabricated using the 1-day-old solution. They also produce an anodic onset potential shift of 260 mV. This improved photoelectrocatalytic response is due to the porous morphology of the films, which produces a larger surface area that enhances light absorption, increases active sites for catalytic reactions, and reduces charge transfer resistance at the photocathode-electrolyte interface.

1. Introduction

The search for favorable photo-catalysts that can drive the photoelectrochemical (PEC) evolution of hydrogen from water has intensified in recent years. This is due to the increasing global quest for suitable renewable energy sources that can replace the widely consumed fossil fuels, which are harmful to the environment.[1] Solar radiation has been regarded as one of the most ideal power sources capable of replacing the commonly consumed fossil fuels.[2] This is because solar radiation is abundant, free, and has very little negative effects on the environment.[3] Solar energy is mainly harnessed through the use of photovoltaic systems to obtain electric power,[4] solar thermal devices to generate heat, as well as electricity,[5] and solar-to-fuel conversions such as the photo-electrolysis of water to produce hydrogen (H$_2$).[6] The photo-electrolysis of water commonly regarded as photoelectrocatalytic water-splitting is a globally desired technology for PEC H$_2$ production.[7] CuO is one of the widely investigated photocathodes for water-splitting applications. This is because it can absorb light in the visible spectrum due to its low bandgap of 1.2–1.7 eV,[8] has a suitable band position for H$_2$ evolution,[7] it's abundant,[9] and promises a solar-to-hydrogen (STH) conversion efficiency of ≈30%.[10]

Many solution-based techniques, such as spin-coating,[11] dip-coating,[12] spray pyrolysis,[13] electrodeposition,[14] successive ionic layer adsorption/reaction,[15] and hydrothermal deposition,[16] have been engaged for preparing CuO films for catalytic purposes. Generally, the techniques first involve the preparation of a precursor solution, which is then used to prepare CuO films via the different deposition approaches. The film's processing parameters, such as precursor concentration, deposition time, drying, and annealing conditions, have been employed in tuning the properties of the CuO films for PEC applications. Kushwaha et al. 2017, obtained two different structures of nanosheets and nanoleaves for hydrothermally deposited CuO photocathodes, by simply varying the precursor concentration used for the film's preparation.[17] Elsewhere, the unwanted surface defects of electrodeposited CuO photocathodes were inhibited through the optimization of electrodeposition time.[18] In our previous study, the engagement of a three-step heating process enhanced the crystallinity and reduced the agglomeration of dip-coated CuO nanoparticles, improving their PEC properties.[12]

P. I. Kyesmen, M. Diale
Department of Physics
University of Pretoria
Private Bag X20, Hatfield 0028, South Africa
E-mail: pannan.kyesmen@up.ac.za; mmantsae.diale@up.ac.za
N. Nombona
Department of Chemistry
University of Pretoria
Private Bag X20, Hatfield 0028, South Africa

**ADVANCED
SCIENCE NEWS**

www.advancedsciencenews.com

**ADVANCED
MATERIALS
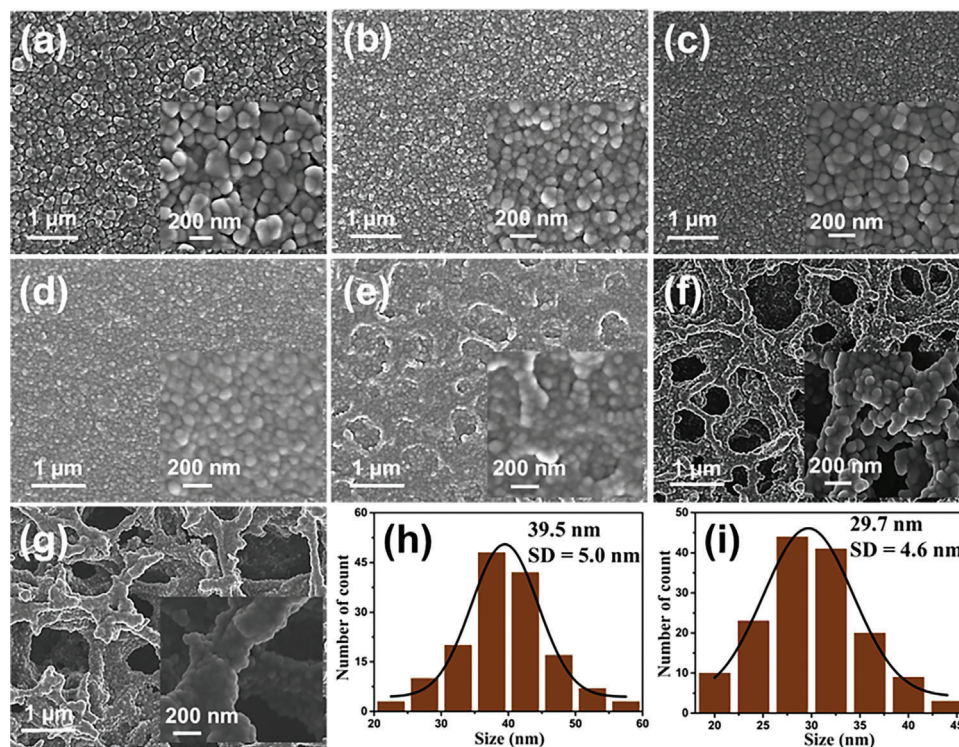INTERFACES**
Open Access

www.advmatinterfaces.de

Figure 1. The surface image of a) CuO-1d, b) CuO-40d, c) CuO-80d, d) CuO-120d, e) CuO-150d, f) CuO-180d, and g) CuO-250d films: the insets present the micrographs of the samples at a larger magnification, while (h) and (i) presents the histograms for the average particle diameter distribution for CuO-1d and CuO-180d films, respectively.

PEC reactions occur on the surface of photoelectrodes during water splitting. Hence, the majority of solution-based techniques for preparing photoelectrodes are geared toward tuning surface properties, such as grain size, surface roughness, and porosity, which serve critical roles in determining PEC response. The introduction of suitable structural defects to a material in the form of a porous geometry has proven to be very effective at boosting the PEC efficiency of photoelectrodes. This is an established aspect of defect engineering that increases a material's surface area and reduces the distance between the charge carriers and the electrolyte.[19]

Numerous surface engineering concepts have been employed in tuning the surface properties of photoelectrode materials toward obtaining suitable nanostructures for enhancing photocatalytic and PEC reactions. Porous electrodeposited CuO photocathodes have been prepared through the optimization of applied potential and deposition time, producing a 1.6-fold enhancement in photocurrent density over the non-porous films at 0.1 V versus RHE.[20] The precursor aging concept has also been engaged in modifying the surface properties of materials for catalytic applications. Byun et al. 2020, prepared $BiVO_4$ films via the metal-organic decomposition method and obtained rougher films and smaller grain sizes after aging the solution used for the synthesis for 1–5 days, achieving the optimum PEC response for the ones fabricated using the 3-day-old solution.[21] Elsewhere, Kumar et al. 2020 achieved a 5.6 times enhancement in the porosity of ZrO_2 films, after sol-aging for 10 days: significant progress toward improving their PEC activity.[22] In another study, electron-gun deposited WO_3 has been reported to form larger aggregates

and rougher surfaces with an increasing aging time of 1–122 h of the precursor solution, producing an enhanced electrochemical response.[23] The precursor aging method has been effective at influencing the surface properties of materials for improved PEC response. However, the method has been widely ignored and not well engaged in tuning the surface properties of dip-coated CuO films for PEC applications.

In this paper, the precursor aging approach was extensively engaged in tuning the surface properties of dip-coated copper (II) oxide (CuO) photocathodes. CuO photocathodes were prepared using Cu-based precursor solutions that were aged for 1–250 days, yielding highly porous, rougher, and better photoresponse for the samples fabricated using the (180–250)-day-old solutions. This research introduces a cheap and easy solution aging method for fabricating suitable dip-coated CuO-based materials for photoelectrocatalytic, photo-sensing, optoelectronics, and photovoltaic applications.

2. Results and Discussion

2.1. Morphological Studies and Elemental Content

The surface microstructures of the fabricated CuO photocathodes are given in **Figure 1**a–g for CuO films prepared using the precursor solution that were aged for 1–250 days. All the prepared films consist of compact spherical nanoparticles with their grain sizes reducing with the aging time of the precursor solution used for film deposition. The histograms for the average particle size distribution for all the CuO samples are given in
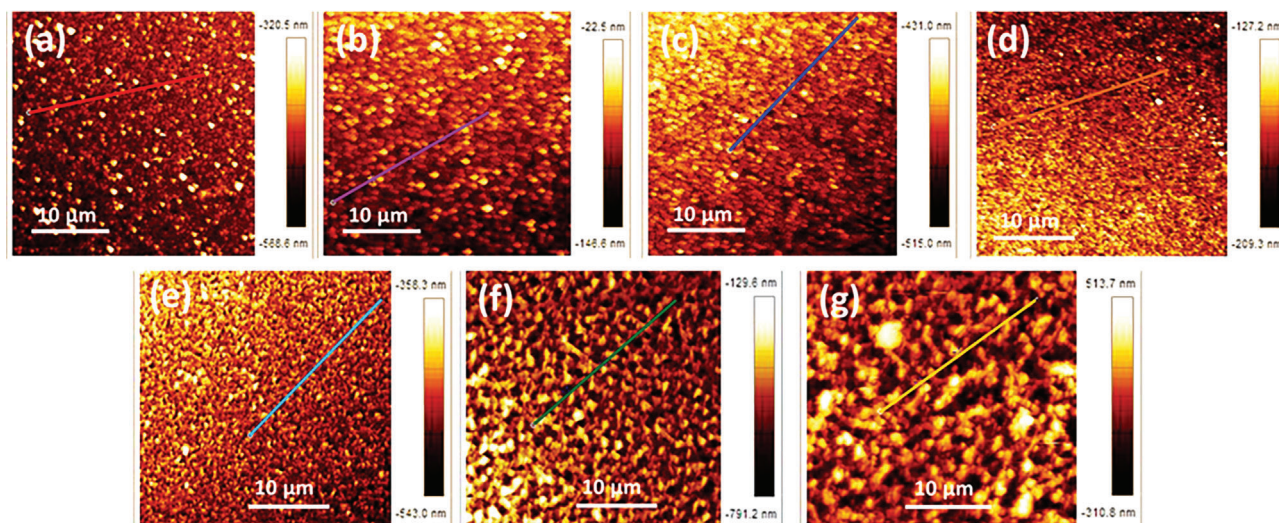
Figure 2. The surface topography of a) CuO-1d, b) CuO-40d, c) CuO-80d, d) CuO-120d, e) CuO-150d, f) CuO-180d, and g) CuO-250d films.

Figure S1, Supporting Information. The histograms for CuO-1d and CuO-180d are presented in Figures 1h,i, respectively, for easy comparison. CuO-1d samples, prepared using the solution that was aged for 1 day, had the highest grain size of 39.5 nm, which reduces by 24.8% and 32.1% for CuO-180d and CuO-250d samples, respectively.

The surface morphology of the CuO films was notably influenced by the aging of the precursor solution. CuO-1d films revealed compact and homogeneous nanoparticles on the film's surface with some slight agglomeration of the particles. The film's surface became more homogeneous and less agglomerated with an increasing precursor aging time of up to 120 days. After precursor aging for 150 days, the prepared CuO films disclosed a uniform surface with some shallow pores. The CuO samples prepared using precursor solution that was aged for 180 days showed a completely porous morphology with an estimated average pore diameter of 623 nm. Further aging of the deposition precursor solution to 250 days also yielded CuO films of porous morphology with relatively larger pores with a mean diameter of 749 nm. However, CuO-250d films revealed a more coalesced surface relative to the CuO-180d samples. Porous surfaces are desired for PEC applications because they provide larger surface areas and more reaction centers during catalytic reactions.[24]

The cross-sectional images of the fabricated CuO films were examined to obtain their estimated film thicknesses. Figure S2a–g, Supporting Information, shows the cross-sectional views for CuO films that were fabricated using the precursors that were aged for 1–250 days. The images were analyzed using ImageJ software to extract the approximate thicknesses of the films. The analysis disclosed films of similar thicknesses of about 372 ± 38 nm for all the prepared CuO films. Precursor aging time did not show any significant impact on the thickness of the deposited films. If the thickness of the prepared CuO films had varied significantly, it can influence photon absorption,[12,25] as well as charge recombination in the bulk of the films, due to the short diffusion length of CuO (≈200 nm).[26] It was therefore valuable that identical thicknesses were obtained for the CuO films to enable a more accurate comparison of their PEC properties.

Atomic force microscopy (AFM) analysis was performed on the CuO films to extract information on the effect of precursor aging on the roughness and porosity of their surface topographies. The topographical images of the prepared films are presented in **Figure 2**a–g. The images disclosed uniformly distributed nanoparticles on the surface of all the films. The results of the roughness analysis conducted on the films are presented in **Figure 3**a. An approximate surface roughness of 29 nm was obtained for the CuO-1d films. Further precursor aging between 40 and 120 days resulted in a notable drop in the surface roughness of the CuO films to a value ranging from 7.8–12 nm with the least value estimated for the CuO-80d films. The reduction in the surface roughness observed for the films was a result of the drop in the grain sizes estimated for the CuO-40d, CuO-80d, and CuO-120d samples relative to CuO-1d (Figure 1), similar to previous reports.[27] This is because smaller grains can decrease the coercivity of nanoparticles, which will result in the formation of smoother films.[28] The surface roughness significantly improved to 20.9 nm for the CuO-150d films. This enhancement was because of the initial inducement of pore formation on the film's surface after precursing aging for 150 days. This is more clearly seen in the scanning electron microscopy (SEM) micrograph image of the film given in Figure 1e. The surface roughness dramatically increased for CuO-180d and CuO-250d photocathodes relative to CuO-1d, attaining a 3- and 4.2-fold increment, respectively. This was a result of the formation of large pores on the surface of the films. The line scans done on the surface of all the films over a 22 µm length are given in Figure 3b and agree well with the roughness analysis conducted on the film's surface. Rougher topographies have been shown to promote electrochemical activity at the photo-catalyst/electrolyte interface for improved PEC response.[29]

Energy dispersive X-ray spectroscopy (EDS) analysis was conducted to investigate the elemental content of the fabricated CuO films and their distribution across the surface of the samples. **Figure 4**a–d shows the elemental distribution for CuO-1d, CuO-150d, CuO-180d, and CuO-250d samples. The distribution of the constituent elements of CuO on the film's surfaces was
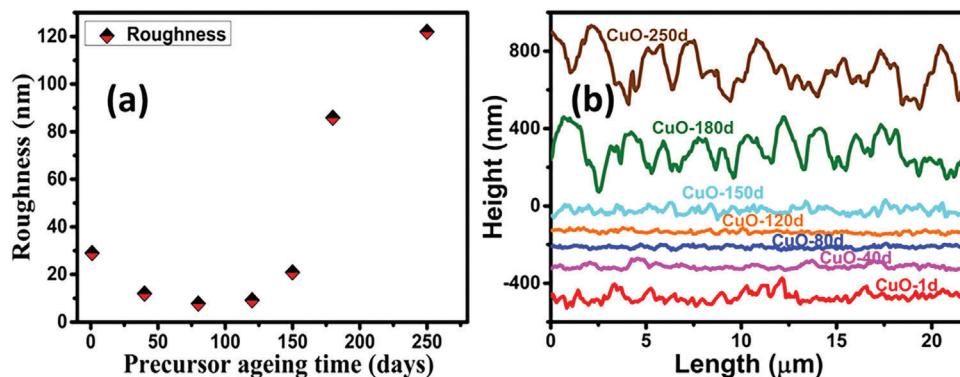
**ADVANCED
SCIENCE NEWS**

www.advancedsciencenews.com

**ADVANCED
MATERIALS
INTERFACES**

Open Access

www.advmatinterfaces.de

Figure 3. The a) roughness values and b) line scan data obtained for CuO films prepared using precursor solution that was aged for 1–250 days.

investigated, as well as that of Sn; one of the key contents of the fluorine-doped tin oxide (FTO) substrates used for film deposition. The analysis revealed a homogeneous distribution of O and Cu on the surface micrographs of the films with some dark regions observed around the porous sites on the surfaces of CuO-180d and CuO-250d samples. The Sn content around the porous regions on the surfaces of CuO-180d and CuO-250d samples became more pronounced because of the proximity of those areas to the FTO substrates. The supplementary data gives the elemental distribution of CuO-40d, CuO-80d, and 120d, showing similar surface and elemental distribution with those of CuO-1d films. The elemental EDS point scans performed also affirmed the presence of Cu, O, and Sn in the films (Figure S3d, Supporting Information). A little amount of Si was observed in the point scans because of the quarts in glass, which was part of the FTO/glass substrates used for film deposition.

2.2. X-ray Diffraction Studies

The X-ray diffraction (XRD) patterns of the CuO films were obtained to ascertain their crystal phase and microstructural proper-

ties. The XRD patterns obtained for the fabricated CuO samples are given in **Figure 5**. The patterns disclosed peaks at (111) and ($\bar{1}$11) planes, in agreement with the tenorite crystal structure of CuO with lattice parameters a = 4.64 Å, b = 3.4 Å, c = 5.09 Å, β = 99.5° (JCPDS no 05–0661). Peaks that belong to Cu and other forms of its oxides were not seen in the XRD patterns, which implied that the CuO samples prepared were of good purity. The peaks at ($\bar{1}$11) were analyzed to ascertain their full width at half maximum (FWHM) and the crystal size (D) for all the prepared CuO films using the Debye–Scherrer approximation. Additional microstructural information was obtained from the microstrain (ε) and the dislocation density (d), evaluated for the CuO samples using Williamson and Smallman's approximation.[30]

The data extracted from the crystal size analysis of the CuO films are presented in **Figure 6**a. The crystal size of the films generally reduces with the aging time of the precursor used for film deposition. The lowest crystal size of 12.9 nm was evaluated for the CuO-250d samples, representing a 37.1% reduction when compared to the value evaluated for CuO-1d films. The reduction of crystal size of the films with precursor aging time eventually resulted in the formation of large pores for CuO-180d and
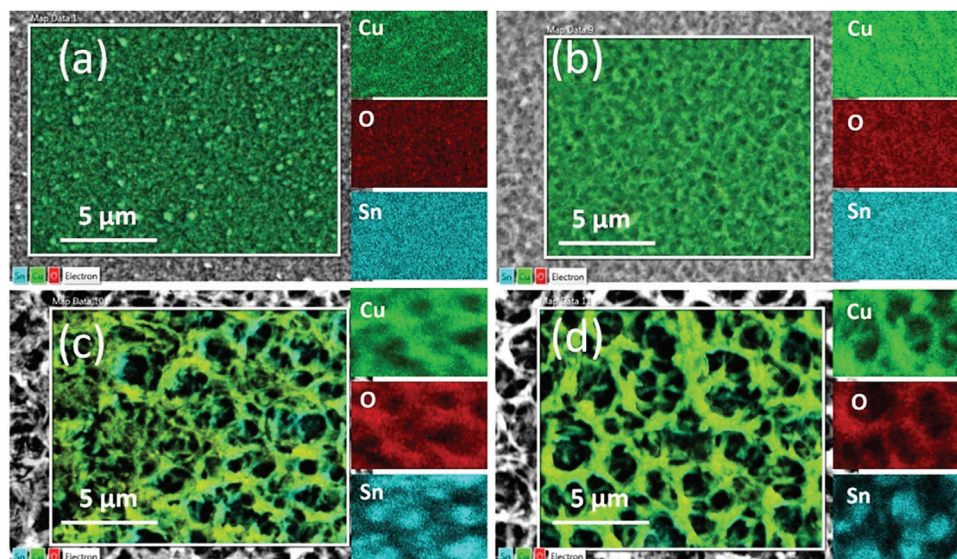

Figure 4. The EDS elemental distribution for a) CuO-1d, b) CuO-150d, c) CuO-180d, and d) CuO-250d samples.

ADVANCED
SCIENCE NEWS
www.advancedsciencenews.com

**ADVANCED
MATERIALS
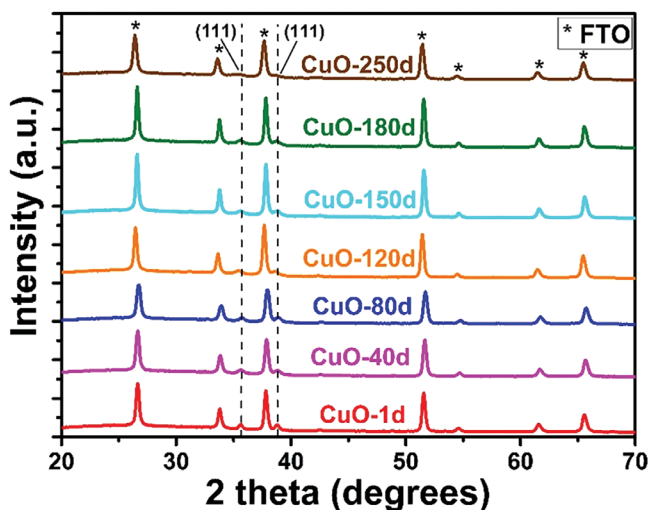INTERFACES**
Open Access
www.advmatinterfaces.de

Figure 5. XRD patterns of dip-coated CuO films prepared using a precursor solution that was aged for 1–250 days.

CuO-250d films: an essential property in photoelectrocatalytic applications.[31]

The microstrain evaluated for the films generally increases with the increasing aging time of the precursor used for film deposition, yielding a maximum value of 8.82×10^{-3} for the CuO-250d films. This represents a 1.6-fold increase when compared to the value evaluated for the CuO-1d films. The observed increase in the microstrain was attributed to an increment in the lattice defects of the films, resulting from the reduction of the crystal size of the samples.[32] Similarly, the dislocation density obtained for the CuO samples generally increases with the aging time of the precursor solution. This is associated with the enhancement of grain boundaries due to the lowering of the crystal size of the films with precursor aging.[33] The highest d value of 6.04×10^{15} lines/m² was obtained for the CuO-250d films, which was 2.5 times higher than what was recorded for CuO-1d samples. The formation of large pores on the surface of CuO-180d and CuO-250d films may have introduced more structural defects, contributing to the high d values evaluated for the films.

2.3. Optical Properties

The optical absorption and the direct and indirect bandgap of the prepared CuO films were obtained from the UV–vis studies performed on the samples. The film's absorption patterns are given in **Figure 7**a. The films exhibited an absorption onset that ranges from 872 to 954 nm, absorbing photons in the visible and some parts of the infrared region of the electromagnetic spectrum. CuO-1d, CuO-40d, CuO-80d, and CuO-120d samples displayed similar absorption patterns. For these films, the decrease in grain size of the films with precursor aging time was accompanied by the reduction in particle agglomeration on the film's surface. Grain size decrease can reduce light absorption,[34] while the reduction in particle agglomeration can enhance it.[35] The effect of these two properties may have counteracted each other, leading to the identical absorption patterns observed. A notable

increase in the roughness of the CuO-150d films coupled with the initial inducement of pores on their surface noticeably enhanced the photo absorption of the films. CuO-180d and CuO-250d displayed a significantly higher optical absorption relative to all the other films. The pores on these film's surfaces induced some light scattering that prolong the photon pathway in the films, yielding the enhanced optical absorption observed.[36] This resulted in the red-shifting of the onset absorption wavelength from 890 nm for CuO-1d films to 953 ± 4 nm for the porous CuO-180d and CuO-250d samples.

The direct and indirect bandgap of the CuO films were evaluated from their measured absorption spectra using the Tauc method given by Equation (1)

$$\alpha h\nu = A(h\nu - E_g)^n \tag{1}$$

where $h\nu$ is the Planck energy, A denotes a constant determined based on the film's thickness, E_g is the bandgap, and n represents a constant that can have values of either 2 or 1/2 for allowed indirect and direct transitions, respectively.[37] The approximated direct and indirect bandgaps of the prepared CuO films are presented in Table S1, Supporting Information. An identical bandgap value of 1.32 ± 0.02 eV was estimated for CuO-1d, CuO-40d, CuO-80d, and CuO-120d films. This agrees with the similar absorption spectra observed for the samples. Further aging of the precursor solution before film deposition led to a drop in the bandgap of the films to 1.27 eV for CuO-150d samples and 1.20 ± 0.03 for CuO-180 and CuO-250d films. The eminent red-shifting of the absorption onset observed for the CuO-180d and CuO-250d films due to the porous nature of their surfaces, broadens their absorption band toward higher wavelengths, causing the reduction of their bandgaps.[38] The lowered bandgap and enhance photon absorption observed for CuO-180d and CuO-250d samples will enhance the generation of photo-induced electron-hole pairs if used as a photo-catalyst: vital for photo applications.[39]

To further understand the contributions of precursor aging in inducing porous surface defects which consequently lead to the bandgap reduction of the CuO films, the UV–vis absorption spectra of the aged precursor solutions were investigated. The absorption patterns of the solutions are given in **Figure 8**. The spectra revealed absorption peaks at 285 and 693 nm for the 1-day aged Cu solution. The peak at 285 nm gradually red-shifted while the one at 693 nm remained the same with precursor aging time. This peak shift was an indication of the displacement of acetate ions with diethanolamine. A color change from blue to dark green was also observed for the solution after aging for 150 days and above, further confirming the formation of the bis-(diethanolamine) copper (II) complex. This complexation reaction is a gradual process which can be more clearly seen in the peak shifts presented in the expanded view of the UV–vis absorption spectra shown in Figure S4, Supporting Information. The formation of large pores on the surfaces of CuO-180d and CuO-250d samples after film deposition and crystallization was associated with the elongated diethanolamine ligand formed in the aged copper solutions, which is longer than the initial acetate ligand. Similar observations have been made for MOFs where more elongated ligands resulted in the emergence of larger pores.[40]
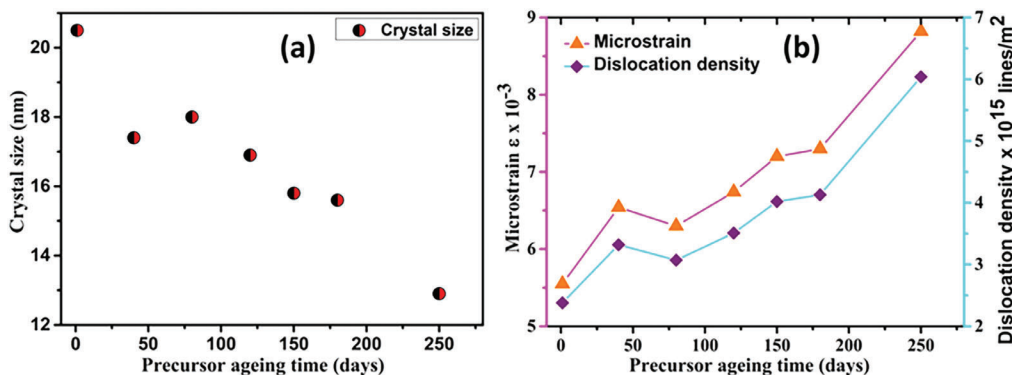
Figure 6. a) Crystal size, and b) microstrain and dislocation density of dip-coated CuO films prepared using precursor solution that was aged for 1–250 days.
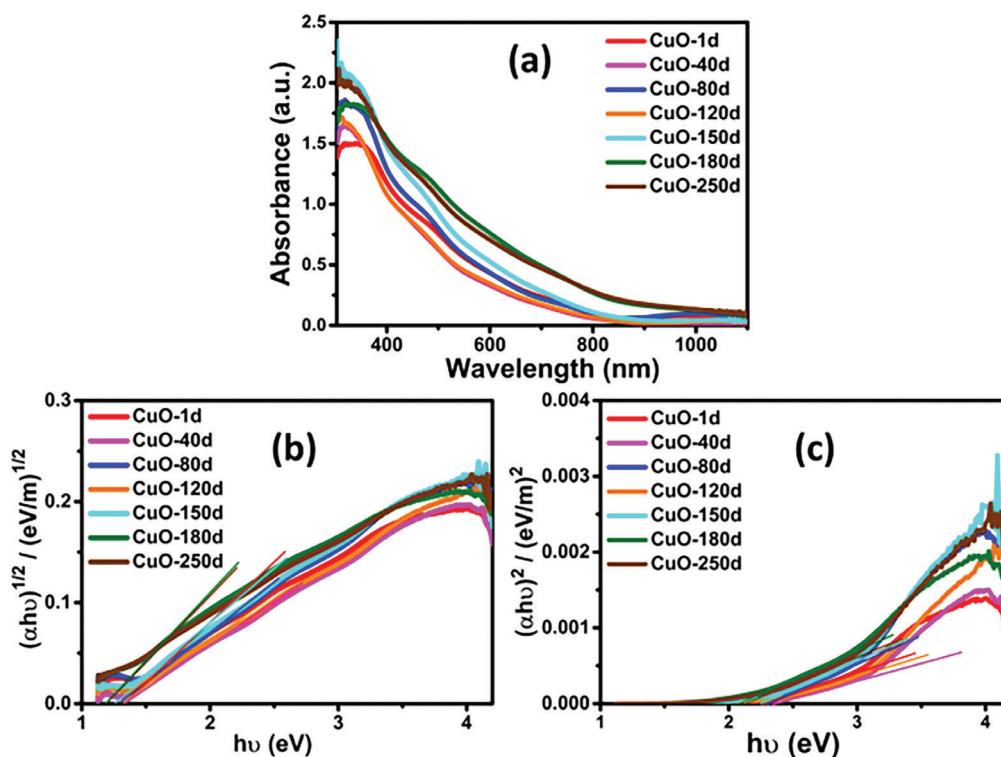

Figure 7. UV–vis a) absorption spectra, b) indirect bandgaps, and c) direct bandgaps of the dip-coated CuO films prepared using precursor solution that was aged for 1–250 days.

2.4. Mott–Schottky Analysis

Mott–Schottky (MS) measurements were conducted on the CuO photocathodes to obtain valuable insights into the effect of precursor aging on the acceptor density (N_A), flat band potential (V_{fb}), and the energy band positions of the films. The MS plots obtained for the photocathodes displayed a negative slope (**Figure 9**), which is a known behavior of the space charge layer of p-type materials such as CuO.

The N_A and V_{fb} values of the CuO films were extracted from the MS plots using the MS formula for p-type semiconductors presented in Equation (2).[41]

$$\frac{1}{C^2} = \frac{2}{\varepsilon_0 \varepsilon e A^2 N_A} \left(-V + V_{fb} - \frac{KT}{e} \right) \qquad (2)$$

where C is the capacitance of the space charge layer, e represents the electronic charge, K stands for the Boltzmann constant, V is the applied potential, A represents the electrode's surface area, T is the temperature, the dielectric constant ($\mathcal{E}$) of the CuO films is 18.1,[13] and ϵ_0 is the vacuum permittivity. The intersection of fitting the linear region of the MS plots on the voltage axis, at

**ADVANCED
SCIENCE NEWS**

www.advancedsciencenews.com

**ADVANCED
MATERIALS
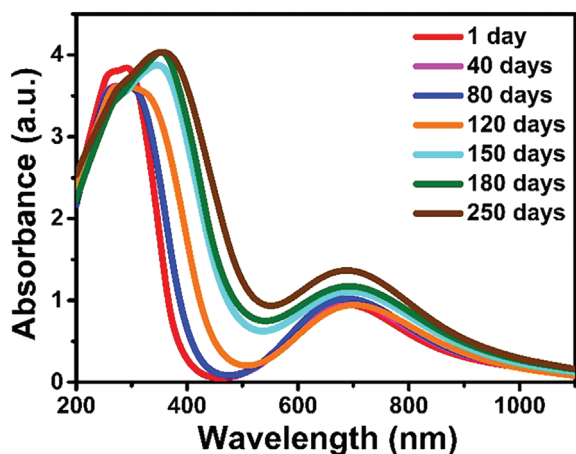INTERFACES**
Open Access

www.advmatinterfaces.de

Figure 8. UV–vis absorption spectra of copper-based solution aged for 1 to 250 days.

$1/C^2 = 0$ was used to deduce the approximate values of V_{fb} for the CuO photocathodes. In addition, the slope of the linear portions of the MS plots was used to get the N_A values of the CuO photocathodes in line with Equation (3) extracted from Equation (2). The N_A and V_{fb} values evaluated for the CuO photocathodes are presented in Table S2, Supporting Information.

$$N_A = -\frac{2}{\varepsilon_0 \varepsilon e A^2} \left[\frac{dV}{d\left(\frac{1}{C^2}\right)} \right] \tag{3}$$

The approximate N_A values evaluated for the prepared CuO samples were in the order of 10^{20}, identical to other acceptor concentration values reported for the films.[42] The maximum N_A value of 8.3×10^{20} cm^{-3} was observed for the CuO samples made from the precursor solution that was aged for 180 days, representing a 2.5-fold increase in comparison with the value obtained for the CuO-1d samples. The notable increase in the N_A value of CuO-180d is linked to the porosity of the film's surface, which greatly suppress charge recombination, enhancing the ac-
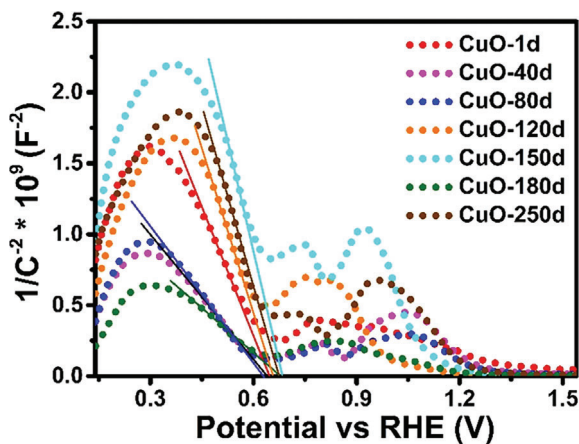

Figure 9. MS plots for the CuO photocathodes prepared using the precursor solution that was aged for 1 to 250 days.

ceptor density.[42a] The CuO-250d samples yielded a much lower N_A value of 2.1×10^{20} cm^{-3} despite having a porous surface. This was attributed to the coalescing of the nanoparticles on the film's surface (Figure 1g), which created charge recombination sites that limits the acceptor concentration of the films.

The V_{fb} values calculated for the CuO films deposited using the precursor solution that was aged between 1 and 120 days yielded identical values of 0.652–0.696 V versus RHE. The V_{fb} values notably shifted to more positive potentials for the CuO photocathodes prepared using the precursor that was aged for 150 days and above. A more positive V_{fb} value is desirable for the film's use in PEC applications. This is because it will produce a larger degree of band bending at the electrode's surface and a wider space charge region, generating a larger driving force that will improve the charge carriers' separation during photoelectrocatalysis.[10,43] Furthermore, the energy band positions for the valence band (E_{VB}) and conduction band (E_{CB}) were estimated using the indirect bandgap evaluated for the films (Figure 7b and Table S1, Supporting Information) and their V_{fb} values. Under the flat band conditions, for a p-type semiconductor, the fermi level (E_f) is taken as the V_{fb} value of the material.[43,44] More so, based on previous studies for a p-type semiconductor, an empirical approximation of 0.20 was estimated as the potential difference between the E_{VB} and E_f positions.[44,45] The E_{VB} of the photocathodes were deduced from their V_{fb} and the E_{CB} positions using the relation: $E_{VB} = E_{CB} + Eg$.[44] The valence and conduction band positions obtained for the films are presented in Table S2, Supporting Information. Comparable E_{VB} values of 0.85–0.93 V versus RHE were evaluated for the photocathodes. These values are similar to other valence band positions reported for CuO films in literature.[43,46] The conduction band position calculated for the films prepared using the precursor solution that was aged for 1 to 120 days were similar, yielding an estimated E_{CB} value of −0.46 ± 0.02 V versus RHE. A comparable E_{CB} value of −0.48 V versus RHE has also been reported for CuO films elsewhere.[46] After precursor aging for 150–250 days, the films produced recorded more positive E_{CB} values, ranging from −0.29 to −0.34 V versus RHE, with CuO-180d photocathodes having the largest shift. This drop in E_{CB} is attributed to the quantum confinement effects resulting from the significant reduction in the grain size of the films, similar to a previous observation for Ge.[47] This shows that the conduction band of the dip-coated CuO films could be tuned through the aging of the precursor solution used for film deposition. For PEC applications, a more positive E_{CB} is an advantage as it shifts the position of the energy band closer to the hydrogen evolution potential, reducing the potential required to drive the electrochemical reaction.

2.5. Impedance Spectroscopy Analysis

Electrochemical impedance spectroscopy (EIS) measurements were performed on the dip-coated CuO photocathodes to study the influence of precursor aging on the charge transfer dynamics occurring at the surface and in the bulk of the samples. The Nyquist plots of the CuO photocathodes obtained from the EIS analysis under light conditions are given in **Figure 10**. The equivalent circuit presented in the inset of Figure 10 was used to model the EIS data recorded for the films. The circuit component, Rs,
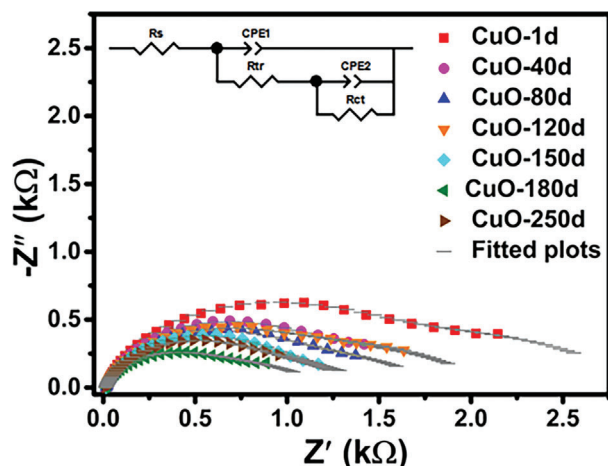
**ADVANCED
SCIENCE NEWS**

www.advancedsciencenews.com

**ADVANCED
MATERIALS
INTERFACES**

www.advmatinterfaces.de

Figure 10. The Nyquist plots of dip-coated CuO films prepared using precursors that were aged for 1–250 days: the colored shaped lines give the plots of the data collected from the raw EIS measurements while the grey lines present the corresponding plots obtained from fitting the data to the equivalent circuit, presented in the inset of the graph.

stands for the series resistance linked to the FTO/CuO interface, the wires connected to the potentiostat, and the electrolyte's ionic conductivity.[48] Rtr stands for the resistance of the trap states in the bulk of the photocathodes while Rct denotes the resistance to charge transfer at the photocathode/liquid junction. The capacitance of the space charge layer is represented by the constant phase element, CPE1, and that of the surface states is symbolized with CPE2. The approximate values deduced for the various elements after fitting the modeled circuit with the EIS data are displayed in **Table 1**. The CPE elements consist of two parts: the pseudo capacitance given by CPE-T, commonly called the Q-value, and the second component, CPE-P, which can have values between 0 and 1. The CPE-P values depict the depressed semicircle seen in the Nyquist plots of the photocathodes.[49] The estimated values for the CPE elements which depict the non-ideal capacitive response of the photocathodes were converted to their actual capacitance (C) values using Equation (4).[50]

$$C = Q^{1/n} \times R^{(1-n)/n} \tag{4}$$

Table 1. The evaluated values for the components in the modeled equivalent circuit that was used to represent the EIS data obtained for the CuO photocathodes.

Sample	Rs [Ω]	CPE1		Cb [mF]	Rtr [kΩ]	CPE2		Cs [mF]	Rct [kΩ]
		T [mF]	P			T [mF]	P		
CuO-1d	13.8	0.30	0.81	0.25	1.51	3.5	0.50	17.15	1.40
CuO-40d	13.8	0.41	0.85	0.35	1.10	4.6	0.50	21.46	1.01
CuO-80d	14.3	0.65	0.82	0.59	0.96	5.2	0.47	28.15	0.86
CuO-120d	13.7	0.65	0.81	0.59	0.99	4.7	0.50	24.30	1.10
CuO-150d	13.3	1.13	0.81	1.10	0.79	5.3	0.42	33.69	0.72
CuO-180d	13.6	1.19	0.85	1.11	0.55	6.4	0.45	36.89	0.66
CuO-250d	14.1	1.22	0.83	1.20	0.74	6.1	0.44	38.00	0.69

where R is the resistance connected in parallel with the CPE elements. The results obtained for the actual capacitance represented as Cb and Cs for CPE1 and CPE2, respectively, and the approximate values of all the elements in the modeled circuit are presented in Table 1.

The series resistance, Rs, obtained in the EIS analysis of the photocathodes yielded similar values of 13.3–14.1 Ω as anticipated since all the films were deposited on FTO substrates and treated under the same heating conditions. The resistance of the trap states in the bulk of the films, Rtr, generally reduces with the aging time of the solution that was used for sample preparation, with the minimum value of 0.55 kΩ observed for CuO-180d. This value represents a 63.6% drop when compared to the maximum Rtr value observed for CuO-1d samples. This means that more of the trap states in CuO-180d films will make it to the solid/liquid junction when compared to the other films, making them more desirable for photoelectrocatalytic applications. The capacitance of the depletion layer in the bulk of the photocathodes (Cb) and that of their surface states (Cs) both increase with the aging time of the solutions that were used for sample preparation. The enhancement of Cs for the films promoted their capability at accumulating surface charge carriers and enhanced their PEC performance.[51] The resistance to the transfer of charge carriers, Rct, yielded the highest value for CuO-1d photocathodes. This limited charge separation on the film's surface and contributed to the low photocurrent response observed for the films in Section 2.6. The Rct values significantly dropped for films fabricated with precursor solution that was aged for 150–250 days, yielding the minimum value of 0.66 for the CuO-180d sample, representing a 52.9% reduction when compared to the estimated value observed for CuO-1d films. The lowered Rct value was due to the high porosity of the CuO-180d films, which increases the number of active sites available for PEC reactions.[52] This reduces the distance that electrons need to travel before making contact with the electrolyte,[53] boosting charge separation and the photocurrent response of the films, as seen in Section 2.6. Additional analysis of the charge transport mechanisms occurring at the surface of the photocathodes is given in the Supporting Information using the Bode plots of log |Z| against log frequency and phase angle versus log frequency shown in Figures S5a and S5b, respectively.

2.6. Photo-Responses

The current response of the prepared CuO photocathodes was studied using linear voltammetry in dark and under illumination conditions and the results are given in **Figure 11**a. No significant dark current response was observed for the films within the potential scan window of 1–0.35 V versus RHE. The CuO-1d photocathode prepared with the deposition precursor solution that was aged for 1d produced the minimum photocurrent density of 0.22 and 0.56 A cm^{-2} at 0.45 and 0.35 versus RHE, respectively. This low photo-response is attributed to the agglomeration of the nanoparticles on the film's surface[54] and the recorded high resistance to charge transport in the bulk of the photocathodes and at the solid/electrolyte junction. Further aging of the precursor solution used for film deposition between 40 and 180 days showed a continuous improvement in the photocurrent
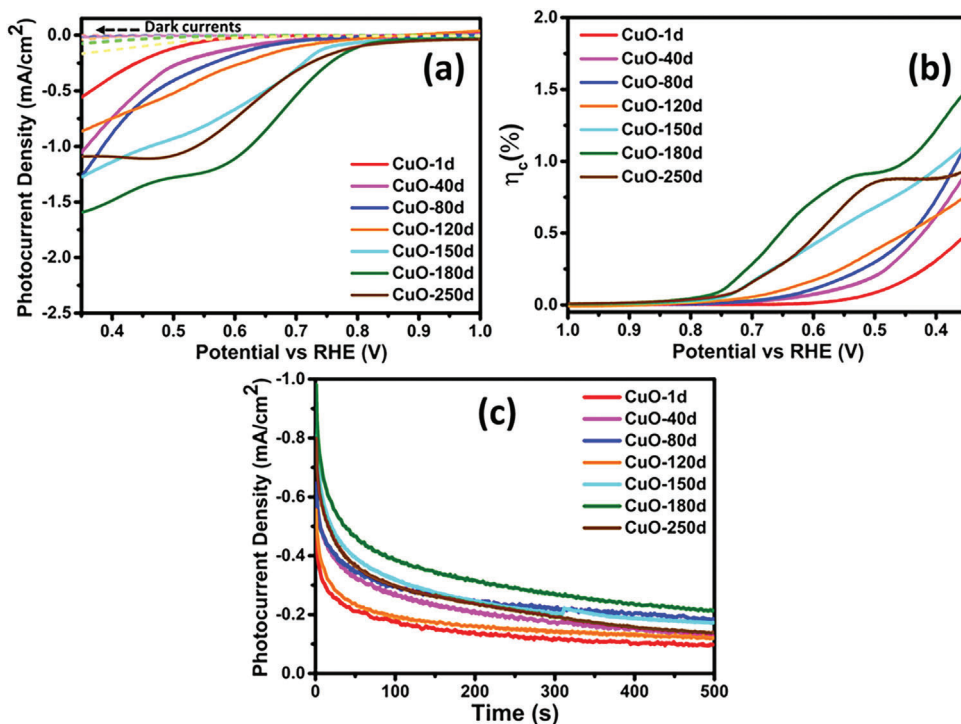
Figure 11. The a) photocurrent density, b) solar conversion efficiency, and c) photostability of CuO photocathodes.

density of the films at 0.45 V versus RHE. The optimum photocurrent density of 1.6 A cm^{-2} was observed for CuO-180d photocathodes at 0.35 V versus RHE, representing a 2.9-fold increase when compared to the CuO-1d samples, at the same potential. This is a very notable photoactivity enhancement for an intrinsic metal oxide that was neither doped nor modified with another material. The photocurrent enhancement was mainly associated with the porous morphology of the films, which increased the number of active sites, lowered the resistance to charge transfer, and greatly reduce charge recombination on the film's surface.[52,53,55] A comparison of the maximum photocurrent density attained by the CuO photocathodes in this project with other reports in the literature is presented in Table S3, Supporting Information. Additional aging of the solution used for sample preparation to 250 days resulted in an 18.4% decrease in the photocurrent density achieved at 0.35 V versus RHE, relative to the observed response of CuO-180 films. This drop was attributed to the coalescing of the film's surface nanoparticles (Figure 1g), which created more charge recombination sites, resulting in increased resistance to charge transfer at the solid–liquid junction. The onset potential for photocurrent yielded a notable anodic shift of over 200 mV for CuO-150d, CuO-180d, and CuO-250d samples with respect to that of CuO-1d. This observation agrees with the more positive V_{fb} values recorded for the films, suggesting a drop in the potential that will be required to initiate PEC reactions.[56]

The approximate solar conversion efficiency (η_{sc}) of the prepared CuO photocathodes was evaluated using Equation (5)

$$\eta_{sc}(\%) = \frac{J_{ph} \times (1.23 - V_{app})}{P_{in}} \qquad (5)$$

where J_{ph} in mA cm^{-2} is the recorded photocurrent density, V_{app} in V versus RHE denotes the applied voltage, and P_{in} (mW cm^{-2}) is the input power of the solar radiation.[57] The conversion efficiencies calculated for the CuO photocathodes are shown in Figure 11b. Precursor aging for 40 days and above generally enhances the η_{sc} of the dip-coated photocathodes. The maximum η_{sc} value of 1.5% was achieved for CuO-180d photocathodes at 0.35 V versus RHE in agreement with the optimum photocurrent density observed for the films. CuO-250d photocathodes produced a 36% drop in the η_{sc} value relative to the evaluated values for CuO-180d films, at the same potential. The higher Rtr and Rct values recorded for the CuO-250d films implied that more charge recombination was occurring in the bulk and surface of the films during photoelectrocatalysis, resulting in the observed drop in η_{sc} for the photocathodes.[58]

The main setback in using CuO as a photocathode in driving PEC reactions is its poor photostability in electrolytes.[59] To test this, a potential-time scan was performed on the films at 0.35 V versus RHE, for 500 s. The photocathodes retained about 35–42.8% of their photocurrent densities after 500 s. CuO photocathodes prepared using the precursors that were aged for 150–250 days exhibited lower photostability due to the drop in the crystallinity of the films (Figure 6a), in line with previously observed results,[60] retaining 31.5% to 34.2% of their photocurrent after 500 s. So, precursor aging resulted in reduced photostability of the CuO photocathodes because of the decreased crystallization of the films. The poor photostability generally observed for the CuO photocathodes is attributed to photo-corrosion, similar to other reports.[59a,61] The photocathodes can be protected with thin layers of stable metal oxides, such as TiO$_2$,[62] metals, such as Ni[57] and Ag,[63] or with a bimetallic material such as Au-Pd,[64] to enhance their photostability in electrolytes.

**ADVANCED
SCIENCE NEWS**

www.advancedsciencenews.com

**ADVANCED
MATERIALS
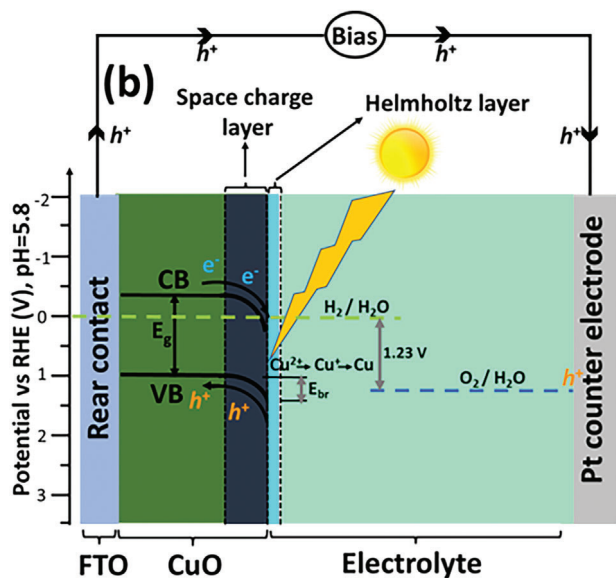INTERFACES**

www.advmatinterfaces.de

Figure 12. Proposed energy band bending, charge transport kinetics, and reaction mechanisms.

The proposed energy band bending, charge transport, and reaction mechanisms occurring on the surface and bulk of the films are displayed in **Figure 12**. If a p-type semiconducting material is dipped into a liquid electrolyte, it will first undergo some charge transfer processes before attaining equilibrium. The ions in the electrolyte are absorbed at the photocathode's interface and the majority of charge carriers around the film's surface, which are holes, in this case, get driven into the electrolyte from the film's surface. This will create a space charge layer around the surface of the films characterize by the absence of holes and the formation of an electric field in the region.[65] The field in this layer will cause the bending of the energy bands downward around the space charge region, in favor of the electron's movement from the CB to the film's surface, and against holes transport to the rear contact from the VB. This will create a potential barrier, Ebr, against hole transport.[66] Concurrently, a region of absorbed ions, adjacent to the electrode's surface is formed, which is often regarded as the Helmholtz layer.[65a]

During photoelectrocatalysis, upon illumination of the photocathodes with photons of energy that are equal to or more than the bandgap of CuO, photogenerated electron–hole pairs are produced. The photogenerated electrons are moved to the CB of CuO and are then transferred to the surface of the photocathodes, where they reduce water to produce H_2. The holes are driven to the VB of CuO and are then moved to FTO rear contact, where they get transported to the counter electrode through the back contact to oxidize water. The separation of charge carriers and their movement to the surface of the photocathodes and FTO contacts are been facilitated by the electric field in the space charge region and the energy band bending. Also, the poor photostability of CuO photocathodes implies that some of the photogenerated electrons at the photocathode's surface will also go on to reduce the CuO to Cu_2O which may be further reduced to Cu if the reaction is prolonged for a sufficient period.[65a,67]

3. Conclusion

In summary, the precursor aging approach was engaged in tuning the surface properties of dip-coated CuO photocathodes for enhanced photoelectrocatalytic activity. A Cu-based precursor solution was aged for 1, 40, 80, 120, 150, 180, and 250 days, and used in each case to fabricate CuO photocathodes on FTO substrates via the dip-coating technique. Compact nanoparticles were observed on the surface of CuO films prepared using the 1-day-old precursor. This was gradually tuned through precursor aging, to produce highly porous and rougher surfaces for the CuO films fabricated using the (180–250)-day-old solutions. The bandgap of the films was also tuned from 1.32 ± 0.02 eV for CuO-1d to 1.20 ± 0.03 for CuO-180 and CuO-250d samples. The optimum photocurrent density of 1.6 mA cm^{-2} at 0.35 V versus RHE was attained for the CuO-180d photocathodes, representing a 196% increase when compared to the value obtained for CuO-1d films, which recorded the least photo response. The photocurrent enhancement was related to the large surface area of the films created by their porous surface, which enhanced light absorption, increased the number of active reaction sites, and reduced the resistance to charge transfer at the solid-liquid interface. This study investigates for the first time, the use of the precursor aging method, in tuning the surface properties of dip-coated CuO films, offering a cheap and easy method for fabricating suitable CuO-based materials for catalytic, optoelectronics, photo-sensing, and photovoltaic applications.

4. Experimental Section

Precursor Preparation and Film Deposition: A previously described method was engaged in the preparation of 0.25 M of copper acetate solution, which was used as the precursor for the fabrication of dip-coated CuO films.[12] In summary, 1.36 g of copper acetate was added to 27 mL of propan-2-ol and stirred for 1 h at room temperature. This was followed by the dropwise addition of 1.5 mL of diethanolamine to the mixture, which was further stirred for 1 h. Finally, 1.5 mL of PEG 400 was added to the suspension and stirred for another 1 h. The resulting solution obtained was initially aged for 1 day and used as the precursor for the preparation of the first set of CuO films on FTO substrates.

For the CuO film deposition, FTO substrates used were first cleaned using a previously described method.[12] The substrates were then dipped into the prepared precursor solution that was aged for 1 day using a PTL-MM01 dip-coater and withdrawn at the velocity of 2 mm s^{-1}. The samples were then dried at 115 °C for 12 min, and heated for another 5 min after heating them to 280 °C. The dip-coating process was repeated four more times to obtain five layers of the deposited films. The samples were then annealed at 550 °C in air, for 1 h, to obtain crystallized CuO films. More CuO films were also produced using the precursor solutions that were aged for 40, 80, 120, 150, 180, and 250 days, respectively. All the CuO films were made to consist of five layers and prepared using the same process described for the samples that were made using the precursor solution that was aged for 1 day. The films prepared using the precursor solutions that were aged for 1, 40, 80, 120, 150, 180, and 250 days were labeled as CuO-1d, CuO-40d, CuO-80d, CuO-120d, CuO-150d, CuO-180d, and CuO-250d, respectively. **Figure 13** presents an illustration of the CuO film fabrication process.

Characterization: The XRD measurements were conducted on the prepared CuO samples to study their structural properties using Bruker D2 PHASER-e diffractometer of Cu-Kα radiation at the wavelength of 0.15418 nm. Field emission gun scanning electron microscopy (FEG-SEM) was performed using the Ultrafast 540 instrument to analyze the surface
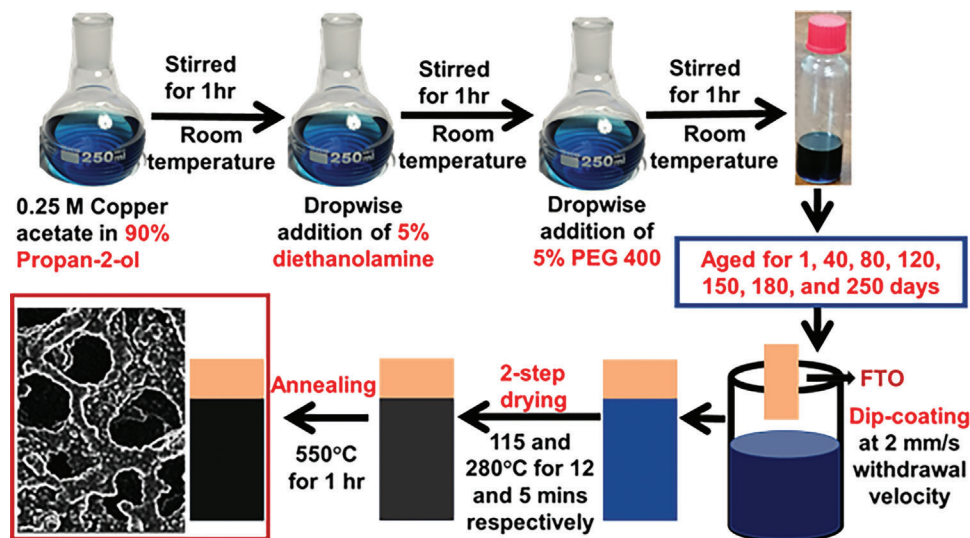
**ADVANCED
SCIENCE NEWS**

www.advancedsciencenews.com

**ADVANCED
MATERIALS
INTERFACES**

www.advmatinterfaces.de

Figure 13. A schematic representation of the procedure used for the preparation of CuO films.

morphology and the cross-sectional images of the CuO films, performed at 2 kV. The Ultrafast 540 microscopy instrument was coupled to EDS, which was used to perform elemental composition analysis on the film's surface, conducted at 20 kV. The films were also studied using the Bruker Dimension Icon with ScanAsyst AFM system, in tapping mode, over the scan area of 30 μm × 30 μm, to further investigate their surface topography. NanoScope Analysis software was used to analyze the AFM images obtained for the films. Agilent CARY 60 UV–vis spectrometer was used to measure the optical absorbance of the CuO films. The UV–vis instrument was used to study the absorption properties of all the aged precursor solutions used in preparing the CuO films. Raman spectroscopy investigations were done on the prepared CuO films using a WiTec alpha300 RAS+ Confocal Raman Microscope with a 532 nm laser at 5 mW.

Electrochemical Measurements: Electrochemical measurements were done using a VersaSTAT 3F potentiostat, which was attached to a PEC cell. The cell consisted of Ag/AgCl in 3 M of KCl, 2 × 2 cm platinum mesh, and the FTO/CuO films as the reference, counter, and working electrodes, respectively. The electrolyte used for the electrochemical studies was 0.5 M Na_2SO_4 (pH = 5.8). Linear sweep voltammetry (LSV) measurements were performed on the CuO photocathodes in dark and light conditions at 0.05 V s^{-1} scan rate to ascertain their photo response. The light source used during the measurements was a Newport *Oriel LCS − 100* solar simulator, under A.M1.5G illumination that was calibrated to 1 sun with a Newport 91 150 V standard cell. The solar simulator was made to consistently illuminate the photocathodes to a limited surface area of 0.49 cm^2. EIS was carried out on all the photocathodes in dark conditions at −0.5 V versus Ag/AgCl, 10 000 to 0.1 Hz of frequency, and an excitation amplitude of 10 mV. ZView software was employed in fitting the data obtained from the EIS measurements to a modeled equivalent circuit. Also, chronoamperometry studies were conducted on the CuO photocathodes in both dark and light conditions at −0.2 V versus Ag/AgCl for a period of 500 s, to investigate their photostability in the electrolyte. The Nernst relation presented in Equation (6) was applied in transforming all the potential versus Ag/AgCl to the RHE scale.

$$V_{RHE} = 0.1976 \text{ V} + (0.059 \times pH) + V_{Ag/AgCl} \tag{6}$$

where V_{RHE} denote the potential versus RHE reference, 0.1976 V is the approximate potential of Ag/AgCl reference against the normal hydrogen electrode (NHE) at 25 °C, and $V_{Ag/AgCl}$ stands for the potential versus Ag/AgCl reference electrode used during the electrochemical measurements.[68]

Supporting Information

Supporting Information is available from the Wiley Online Library or from the author.

Conflict of Interest

The authors declare no conflict of interest.

Data Availability Statement

The data that support the findings of this study are available from the corresponding author upon reasonable request.

[1] K. B. Karnauskas, S. L. Miller, A. C. Schapiro, *GeoHealth* **2020**, *4*, e2019GH000237.

[2] M. B. Hayat, D. Ali, K. C. Monyake, L. Alagha, N. Ahmed, *Int. J. Energy Res.* **2019**, *43*, 1049.

[3] a) K. Solangi, M. Islam, R. Saidur, N. Rahim, H. Fayaz, *Renewable Sustainable Energy Rev.* **2011**, *15*, 2149; b) S. Sen, S. Ganguly, A. Das, J. Sen, S. Dey, *J. Afr. Earth Sci.* **2016**, *122*, 25.

**ADVANCED
SCIENCE NEWS**

www.advancedsciencenews.com

**ADVANCED
MATERIALS
INTERFACES**

www.advmatinterfaces.de

[4] O. Khaselev, J. A. Turner, *Science* **1998**, *280*, 425.

[5] C. Chang, C. Yang, Y. Liu, P. Tao, C. Song, W. Shang, J. Wu, T. Deng, *ACS Appl. Mater. Interfaces* **2016**, *8*, 23412.

[6] S. Ishizuka, R. Okamoto, S. Ikeda, *Adv. Mater. Interfaces* **2022**, *9*, 2201266.

[7] R. S. Moakhar, S. M. Hosseini-Hosseinabad, S. Masudy-Panah, A. Seza, M. Jalali, H. Fallah-Arani, F. Dabir, S. Gholipour, Y. Abdi, M. Bagheri-Hariri, *Adv. Mater.* **2021**, *33*, 2007285.

[8] F. X. Xiao, B. Liu, *Adv. Mater. Interfaces* **2018**, *5*, 1701098.

[9] Y. Shen, M. Guo, X. Xia, G. Shao, *Acta Mater.* **2015**, *85*, 122.

[10] Y. J. Seo, M. Arunachalam, K.-S. Ahn, S. H. Kang, *Appl. Surf. Sci.* **2021**, *551*, 149375.

[11] C.-J. Chang, C.-W. Lai, W.-C. Jiang, Y.-S. Li, C. Choi, H.-C. Yu, S.-J. Chen, Y. Choi, *Coatings* **2022**, *12*, 1206.

[12] P. I. Kyesmen, N. Nombona, M. Diale, *ACS Omega* **2021**, *6*, 33398.

[13] M. Patel, R. Pati, P. Marathey, J. Kim, I. Mukhopadhyay, A. Ray, *J. Electrochem. Soc.* **2016**, *163*, H1195.

[14] M. Izaki, M. Nagai, K. Maeda, F. B. Mohamad, K. Motomura, J. Sasano, T. Shinagawa, S. Watase, *J. Electrochem. Soc.* **2011**, *158*, D578.

[15] X. Tian, Q. Wang, Q. Zhao, L. Qiu, X. Zhang, S. Gao, *Sep. Purif. Technol.* **2019**, *209*, 368.

[16] N. H. Lam, N. T. N. Truong, C. T. T. Thuy, M. S. Tamboli, A. M. Tamboli, J. Jung, K.-s. Ahn, C.-D. Kim, J. H. Jung, *Metals* **2022**, *12*, 484.

[17] A. Kushwaha, R. S. Moakhar, G. K. Goh, G. K. Dalapati, *J. Photochem. Photobiol., A* **2017**, *337*, 54.

[18] A. Mahmood, F. Tezcan, G. Kardaş, *Int. J. Hydrogen Energy* **2017**, *42*, 23268.

[19] W. Q. Fang, Z. Huo, P. Liu, X. L. Wang, M. Zhang, Y. Jia, H. Zhang, H. Zhao, H. G. Yang, X. Yao, *Chemistry* **2014**, *20*, 11439.

[20] M. Basu, *ChemPhotoChem* **2019**, *3*, 1254.

[21] S. Byun, G. Jung, Y. Shi, M. Lanza, B. Shin, *Adv. Funct. Mater.* **2020**, *30*, 1806662.

[22] M. Kumar, G. Reddy, *AIP Adv.* **2011**, *1*, 022111.

[23] M. Giannouli, G. Leftheriotis, *Sol. Energy Mater. Sol. Cells* **2011**, *95*, 1932.

[24] S. Kumar, K. Ojha, A. K. Ganguli, *Adv. Mater. Interfaces* **2017**, *4*, 1600981.

[25] A. A. Al-Ghamdi, M. Khedr, M. S. Ansari, P. Hasan, M. S. Abdel-Wahab, A. Farghali, *Phys. E* **2016**, *81*, 83.

[26] N. D. Khiavi, R. Katal, S. Kholghi Eshkalak, S. Masudy-Panah, S. Ramakrishna, H. Jiangyong, *Nanomaterials* **2019**, *9*, 1011.

[27] E. S. Hassan, A. K. Elttayef, S. H. Mostafa, M. H. Salim, S. S. Chiad, *J. Mater. Sci.: Mater. Electron.* **2019**, *30*, 15943.

[28] a) J. Yi, X. Li, J. Ding, H. Seet, *J. Alloys Compd.* **2007**, *428*, 230; b) B. Yoo, S. Hernandez, D.-Y. Park, N. Myung, *Electrochim. Acta* **2006**, *51*, 6346.

[29] a) A. Sreedhar, I. N. Reddy, Q. T. H. Ta, E. Cho, J.-S. Noh, *Sol. Energy* **2019**, *191*, 151; b) N. Naseri, M. Yousefi, A. Moshfegh, *Sol. Energy* **2011**, *85*, 1972.

[30] R. Nithiyavathi, S. J. Sundaram, G. T. Anand, D. R. Kumar, A. D. Raj, D. A. Al Farraj, R. M. Aljowaie, M. R. AbdelGawwad, Y. Samson, K. Kaviyarasu, *J. Infect. Public Health* **2021**, *14*, 1893.

[31] R. Beissenov, A. Mereke, A. Umirzakov, Z. Mansurov, B. Rakhmetov, Y. Beisenova, A. Shaikenova, D. Muratov, *Mater. Sci. Semicond. Process.* **2021**, *121*, 105360.

[32] a) V. Dhanasekaran, T. Mahalingam, *J. Alloys Compd.* **2012**, *539*, 50; b) K. Maniammal, G. Madhu, V. Biju, *Phys. E* **2017**, *85*, 214.

[33] Z. Landolsi, I. B. Assaker, R. Chtourou, S. Ammar, *J. Mater. Sci.: Mater. Electron.* **2018**, *29*, 8176.

[34] R. Bai, D. Kumar, S. Chaudhary, D. K. Pandya, *Acta Mater.* **2017**, *131*, 11.

[35] a) M. MamathaKumari, D. P. Kumar, P. Haridoss, V. DurgaKumari, M. Shankar, *Int. J. Hydrogen Energy* **2015**, *40*, 1665; b) R. Yang, D. Li, S. L. Salazar, Z. Rao, M. Arıcı, W. Wei, *Sol. Energy Mater. Sol. Cells* **2021**, *219*, 110792.

[36] J. Wang, J. Zhao, Y. Li, M. Yang, Y.-Q. Chang, J.-P. Zhang, Z. Sun, Y. Wang, *ACS Macro Lett.* **2015**, *4*, 392.

[37] P. R. Jubu, O. Obaseki, A. Nathan-Abutu, F. Yam, Y. Yusof, M. Ochang, *Results Opt.* **2022**, *9*, 100273.

[38] B. Kilic, E. B. Simsek, S. Turkdogan, P. Demircivi, Ö. Tuna, S. P. Mucur, D. Berek, *J. Nanopart. Res.* **2020**, *22*, 52.

[39] a) X. Song, X. Liu, D. Yu, C. Huo, J. Ji, X. Li, S. Zhang, Y. Zou, G. Zhu, Y. Wang, *ACS Appl. Mater. Interfaces* **2018**, *10*, 2801; b) D. Wang, C. Huang, X. Liu, H. Zhang, H. Yu, S. Fang, B. S. Ooi, Z. Mi, J. H. He, H. Sun, *Adv. Opt. Mater.* **2021**, *9*, 2000893; c) H. Wang, J. A. Turner, *J. Electrochem. Soc.* **2010**, *157*, F173.

[40] a) D. Gygi, E. D. Bloch, J. A. Mason, M. R. Hudson, M. I. Gonzalez, R. L. Siegelman, T. A. Darwish, W. L. Queen, C. M. Brown, J. R. Long, *Chem. Mater.* **2016**, *28*, 1128; b) S. C. Qi, X. Y. Qian, Q. X. He, K. J. Miao, Y. Jiang, P. Tan, X. Q. Liu, L. B. Sun, *Angew. Chem., Int. Ed.* **2019**, *58*, 10104.

[41] P. P. Sahoo, B. Zoellner, P. A. Maggard, *J. Mater. Chem. A* **2015**, *3*, 4501.

[42] a) C.-Y. Chiang, Y. Shin, S. Ehrman, *J. Electrochem. Soc.* **2011**, *159*, B227; b) J. Deuermeier, H. Liu, L. Rapenne, T. Calmeiro, G. Renou, R. Martins, D. Munoz-Rojas, E. Fortunato, *APL Mater.* **2018**, *6*, 096103.

[43] Y. Yang, D. Xu, Q. Wu, P. Diao, *Sci. Rep.* **2016**, *6*, 35158.

[44] S. Luo, J. Ke, M. Yuan, Q. Zhang, P. Xie, L. Deng, S. Wang, *Appl. Catal., B* **2018**, *221*, 215.

[45] G. Hu, C.-X. Hu, Z.-Y. Zhu, L. Zhang, Q. Wang, H.-L. Zhang, *ACS Sustainable Chem. Eng.* **2018**, *6*, 8801.

[46] H. L. Santos, P. G. Corradini, M. A. Andrade, L. H. Mascaro, *J. Solid State Electrochem.* **2020**, *24*, 1899.

[47] C. Bostedt, T. Van Buuren, T. Willey, N. Franco, L. Terminello, C. Heske, T. Möller, *Appl. Phys. Lett.* **2004**, *84*, 4056.

[48] T. Lopes, L. Andrade, F. L.e Formal, M. Gratzel, K. Sivula, A. Mendes, *Phys. Chem. Chem. Phys.* **2014**, *16*, 16515.

[49] Y. Gönüllü, K. Kelm, S. Mathur, B. Saruhan, *Chemosensors* **2014**, *2*, 69.

[50] B. Hirschorn, M. E. Orazem, B. Tribollet, V. Vivier, I. Frateur, M. Musiani, *Electrochim. Acta* **2010**, *55*, 6218.

[51] a) B. Eftekharinia, A. Moshaii, A. Dabirian, N. S. Vayghan, *J. Mater. Chem. A* **2017**, *5*, 3412; b) B. Klahr, S. Gimenez, F. Fabregat-Santiago, T. Hamann, J. Bisquert, *J. Am. Chem. Soc.* **2012**, *134*, 4294.

[52] S. Shen, J. Jiang, P. Guo, L. Guo, *Int. J. Photoenergy* **2013**, *2013*, 174982.

[53] C.-Y. Chiang, M.-H. Chang, H.-S. Liu, C. Y. Tai, S. Ehrman, *Ind. Eng. Chem. Res.* **2012**, *51*, 5207.

[54] a) F. Pellegrino, L. Pellutiè, F. Sordello, C. Minero, E. Ortel, V.-D. Hodoroaba, V. Maurino, *Appl. Catal., B* **2017**, *216*, 80; b) J. A. Nasir, Z. ur Rehman, S. N. A. Shah, A. Khan, I. S. Butler, C. R. A. Catlow, *J. Mater. Chem. A* **2020**, *8*, 20752.

[55] S. M. Thalluri, R. M. Rojas, O. D. Rivera, S. Hernández, N. Russo, S. E. Rodil, *Phys. Chem. Chem. Phys.* **2015**, *17*, 17821.

[56] a) Y.-C. Lin, L.-C. Hsu, C.-Y. Lin, C.-L. Chiang, C.-M. Chou, W.-W. Wu, S.-Y. Chen, Y.-G. Lin, *ACS Appl. Mater. Interfaces* **2019**, *11*, 38625; b) T.-Y. Yang, H.-Y. Kang, K. Jin, S. Park, J.-H. Lee, U. Sim, H.-Y. Jeong, Y.-C. Joo, K. T. Nam, *J. Mater. Chem. A* **2014**, *2*, 2297.

[57] A. A. Dubale, C.-J. Pan, A. G. Tamirat, H.-M. Chen, W.-N. Su, C.-H. Chen, J. Rick, D. W. Ayele, B. A. Aragaw, J.-F. Lee, *J. Mater. Chem. A* **2015**, *3*, 12482.

[58] Y. Wang, S. Cao, Y. Huan, T. Nie, Z. Ji, Z. Bai, X. Cheng, J. Xi, X. Yan, *Appl. Surf. Sci.* **2020**, *526*, 146700.

[59] a) S. Lee, Y. Hong, H. Ryu, J. Yun, *Thin Solid Films* **2020**, *697*, 137849; b) A. Cots, P. Bonete, R. Gómez, *ACS Appl. Mater. Interfaces* **2018**, *10*, 26348.

ADVANCED
SCIENCE NEWS

www.advancedsciencenews.com

ADVANCED
MATERIALS
INTERFACES
Open Access

www.advmatinterfaces.de

[60] S. Masudy-Panah, R. S. Moakhar, C. S. Chua, H. R. Tan, T. I. Wong, D. Chi, G. K. Dalapati, *ACS Appl. Mater. Interfaces* **2016**, *8*, 1206.

[61] H. Xing, E. Lei, Z. Guo, D. Zhao, X. Li, Z. Liu, *Inorg. Chem. Front.* **2019**, *6*, 2488.

[62] C. Das, B. Ananthoju, A. K. Dhara, M. Aslam, S. K. Sarkar, K. R. Balasubramaniam, *Adv. Mater. Interfaces* **2017**, *4*, 1700271.

[63] X. Zhao, P. Wang, Z. Yan, N. Ren, *Chem. Phys. Lett.* **2014**, *609*, 59.

[64] S. Masudy-Panah, R. S. Moakhar, C. S. Chua, A. Kushwaha, G. K. Dalapati, *ACS Appl. Mater. Interfaces* **2017**, *9*, 27596.

[65] a) P. Dias, A. Mendes, (Ed. R. A. Meyers) Springer Science and Business Media LLC, Springer, Berlin **2017**, p. 1; b) C. Jiang, S. J. Moniz, A. Wang, T. Zhang, J. Tang, *Chem. Soc. Rev.* **2017**, *46*, 4645.

[66] E. Kusmierek, *Catalysts* **2020**, *10*, 439.

[67] Q. Huang, Z. Ye, X. Xiao, *J. Mater. Chem. A* **2015**, *3*, 15824.

[68] A. G. Tamirat, A. A. Dubale, W.-N. Su, H.-M. Chen, B.-J. Hwang, *Phys. Chem. Chem. Phys.* **2017**, *19*, 20881.

2300230 (13 of 13)